

Are stellar mass binary black hole mergers isotropically distributed?

Richard Stiskalek¹, John Veitch¹, & Chris Messenger¹

¹ *School of Physics and Astronomy, University of Glasgow, Glasgow, G12 8QQ, United Kingdom*

ABSTRACT

The Advanced LIGO and Advanced Virgo gravitational wave detectors have detected a population of binary black hole mergers in their first two observing runs. For each of these events we have been able to associate a potential sky location region represented as a probability distribution on the sky. Thus, at this point we may ask the question of whether this distribution agrees with the isotropic model of the universe or if there is any evidence of anisotropy. We perform Bayesian model selection between an isotropic and a simple anisotropic model, taking into account the anisotropic selection function caused by the underlying antenna patterns and sensitivity of the interferometers over the sidereal day. Using the ten binary mergers, we find a Bayes factor of $\sim 16 : 1$ in favour of the isotropic model over a simple pixel-based distribution on the sky. This suggests that the available data from the first two observing runs is better described with an isotropic model. However, the first detections were mostly poorly localised in the sky (before the Advanced Virgo joined the network), spanning large portions of the sky and hampering detection of potential anisotropy. Thus, it would be appropriate to repeat this analysis with events from the ongoing third LIGO observational run and with a more sophisticated cosmological model.

Key words: gravitational waves

1 INTRODUCTION

The first detection of gravitational waves by Advanced LIGO (Abbott et al. 2018; LIGO Scientific Collaboration 2015; Harry 2010; Abbott et al. 2016b), revealed the existence of a detectible population of coalescing stellar-mass binary black holes (BBHs). This was confirmed by subsequent BBH detections in two observing runs (O1 (Abbott et al. 2016a), O2 (Abbott et al. 2017a; Abbott et al. 2017c; Abbott et al. 2017b)), during the latter of which the Advanced Virgo detector joined the network (Virgo Collaboration 2014). The location of the mergers can be determined by performing a coherent analysis of the data from the two-or three-detector network, using either a rapid localisation algorithm (Singer & Price 2016) or a full parameter estimation method (Veitch et al. 2015). Although the initial detections could be constrained to only tens to hundreds of square degrees, the addition of Advanced Virgo to the network has resulted in improved localisation of subsequent detections such as GW170814 (Abbott et al. 2017b).

With 10 BBH detections being announced to date from O1 and O2, it is possible to begin to determine the properties of the source population, such as the rate, sky and mass distribution (Abbott et al. 2016c,a, 2019c). This type of question is addressed by a hierarchical analysis of the sources, which must include the effect of the detector sensitivity on the detectible events. Previous studies have looked at the variation of the selection function with mass, spin, and sidereal time (O’Shaughnessy et al. 2010; Dominik et al. 2015; Ng et al. 2018; Chen et al. 2017). The situation is further complicated by the large uncertainties on the source location, particularly during O1 when only the two LIGO detectors were operational.

Standard cosmological models are consistent with the cosmological principle, that the properties of the universe are the same for all observers when viewed on large scales. One of the two testable consequences of this being that the universe, and as an extension, gravitational wave sources, would be distributed isotropically. Analysis of cosmic microwave background temperature and polarisation fluctuations using Planck observations have concluded that anisotropy is strongly disfavoured (Saadeh et al. 2016). However, gravitational wave observations provide an independent channel through which to verify this conclusion. In addition, current gravitational wave detections and a subset of those expected in the future will likely not satisfy the condition of being viewed at large scales. The largest observed structure (Horvath et al. 2013) (defined by the spatial distribution of gamma-ray burst events) is \sim (Gpc) in size and corresponds to the current most distant detected BBH events. Hence, it will be interesting to study whether the observed sky distribution of gravitational wave events matches that of the local structure seen via electromagnetic channels.

In this work we will address the issue of the distribution of sources over the sky, taking into account the sky-variation of the selection function of the detector network during the first two observing runs. Our intent is to compare two models; an isotropic source population and an anisotropic model that divides the sky into a finite set of pixels. In Section 2 we describe these models together with our analysis, report the results in Section 3 and in Section 4 we summarise the results, discuss the model and its astrophysical significance.

1.1 Data

The posterior samples containing information about the sky localisation of events were taken from the LIGO data releases via the Gravitational-Wave Open Science Center (GWOSC) (Vallisneri et al. 2015), and the following events were used: GW150914, LVT151012, GW151226, GW170104, GW170608, GW170729, GW170809, GW170814, GW170818 and GW170823 (Abbott et al. 2019b). In the subsequent analysis we limit each event to 1000 posterior samples to reduce the computational complexity and weight each event equally. Figure 1 shows a scatter plot of samples from the sky posterior probability densities for all events, binned into 12 pixels. A large proportion of all samples is coming from a single region of the sky (mostly due to GW170814 and GW170809 being tightly localised), whereas some areas of the sky have almost no samples. As for the power spectral density (PSD) curves, we separately consider the PSD estimates at the time of event (LIGO-Virgo Collaboration 2019) and run-averaged (Daniel Sigg 2016a,b; LIGO-Virgo Collaboration 2018) estimates, using the publicly available noise curves (Abbott et al. 2019b).

2 ANALYSIS

Ultimately, the focus of this work is to represent the distribution of BBH sources on the sky. To do so, there are two readily available methods of decomposing the sky into either a finite set of pixels or spherical harmonics. In this work, for simplicity, we opt for a model that decomposes the sky into a finite set of pixels.

In this pixelated anisotropic model we divide the sky into N pixels of equal area $4\pi/N$ steradians. Each pixel i has a parameter a_i (which is further referred to as pixel weight), describing the stellar-mass BBH merger rate per steradian within that pixel. In case of the anisotropic model the number of pixels was chosen to be $N_{\text{ani}} = 12$, since in the subsequent analysis we work with HEALPix maps (Górski et al. 2005) via the Python package Healpy where 12 is the minimum number of pixels available, making the analysis computationally inexpensive, while still ensuring the model has freedom to detect large-scale anisotropy. For the isotropic model we simply use $N_{\text{iso}} = 1$, wherein the whole sky is described by one pixel, ensuring a uniform distribution of the rate of BBH mergers. Given that the pixel weights give the rate per steradian, we also infer the total rate as an integral over the whole sky. Moreover, HEALPix divides the sky into N pixels with a fixed distribution. Therefore to allow for different angular distribution of pixels we introduce three Euler angles $\vec{\phi} \equiv \{\alpha, \beta, \gamma\}$ to describe the reference position and orientation of the HEALPix grid.

We perform a Bayesian analysis to estimate the pixel weights $\vec{a} \equiv \{a_i\}$ and to perform model selection between the isotropic and non-isotropic models. For a given model $I \in \{\text{ISO}, \text{ANISO}\}$, gravitational wave datasets $\{x_j\}$ for each of a number of detections N_{obs} , and where D indicates detection (described in Subsection 2.1), the posterior on the parameters $\vec{\theta} = \{\vec{a}, \vec{\phi}\}$, where \vec{a} are the pixel weights and $\vec{\phi}$ the Euler angles, is given by

$$p(\vec{\theta}|N_{\text{obs}}, \{x_j\}, D, I) = \frac{p(N_{\text{obs}}, \{x_j\}|\vec{\theta}, D, I)p(\vec{\theta}|D, I)}{p(N_{\text{obs}}, \{x_j\}|D, I)}. \quad (1)$$

In this analysis the pixel weights \vec{a} describe the rate of BBH mergers per unit volume (both models assume homogenous distribution of mergers within each pixel), per unit time, per unit steradian, i.e. the units of \vec{a} are $[\vec{a}] = \text{Gpc}^{-3}\text{yr}^{-1}\text{sr}^{-1}$. This allows us to compute the

total rate R ($[R] = \text{Gpc}^{-3}\text{yr}^{-1}$) as

$$R = \Delta \sum_i a_i, \quad (2)$$

i.e. the sum of the product of pixel weights and pixel areas Δ , making R conditionally dependant on \vec{a} . The Euler angles $\vec{\phi}$ are used to calculate a rotation matrix to rotate the GW datasets $\{x_j\}$ to accommodate for different orientations of the fixed HEALPix grid.

Having obtained the expression for the posterior (Eq. 1) we calculate the evidences for each model,

$$p(N_{\text{obs}}, \{x_j\}|D, I) = \int p(N_{\text{obs}}, \{x_j\}, \vec{\theta}, D, I)p(\vec{\theta}|D, I)d^n \vec{\theta}. \quad (3)$$

The ratio of evidences from the two models gives us the Bayes factor between them, indicating the relative support for one over the other that is imparted by a particular set of observations. For the isotropic model there is only pixel, hence one pixel weight a_{iso} related to the total rate as $R = 4\pi a_{\text{iso}}$. Moreover, the isotropic model is also independent of the Euler angles $\vec{\theta}$. We use the nested sampling algorithm (Skilling 2006) implemented in a Python package CPNest (Veitch et al. 2017) to sample the posterior and obtain the evidences.

2.1 Selection function

The selection function describes the interferometer sensitivity for a given distribution of BBH masses as a function of sky position and distance. We consider both the O1 and O2 runs separately and define the selection function following (Abbott et al. 2019a) as

$$p(D|\Omega, d_L, I) = \int_{\rho_{\text{thresh}}}^{\infty} d\rho p(\rho|\Omega, d_L, \vec{\theta}, I)p(\vec{\theta}|\Omega, I)p(d_L|I) \quad (4)$$

where a signal is modelled as detected if its signal-to-noise-ratio ρ is measured above a predefined threshold. The probability of detection, conditional on the sky location, is computed by marginalising over the prior ranges of the distance and the remaining source parameters denoted by $\vec{\theta}$ (inclination, polarisation, etc.). The mass distribution of the primary is assumed to be a power-law $p(m_1) \propto m_1^{-2.35}$, with a minimum mass of $5M_{\odot}$, and the secondary to be uniformly distributed, being always less massive than the primary. Furthermore, a constraint is placed on the sum of the primary and secondary to be always less than $100M_{\odot}$. This choice of BBH mass distribution is consistent with the estimated distribution following the O1 observing run (Abbott et al. 2016a).

Since we are interested in anisotropy, we must consider the directional sensitivity of the detectors. The detectors are most sensitive to sources positioned directly above and below the detector (Anderson et al. 2001). As the Earth rotates, the antennae response function is smeared out in right-ascension, but as noted in (Chen et al. 2017), there is a tendency for the detector sensitivity to vary over the course of the day due to human activity near the sites. This, therefore, produces a selection function which is specific to the observing conditions during a particular observing run. A full treatment of this would need to use the actual noise power spectra as a function of time throughout the observing run, but we approximate this by taking the run-averaged power spectrum, and integrating the antenna response function over sidereal time, using a weight of one when the detector was taking science quality data (Vallisneri et al. 2015). We plot this averaged selection for both observing runs in Fig. 4. The ratio of the maximum and minimum averaged selection function in Fig. 4 is about 1.5 and 1.4 for O1 and O2 respectively, indicating that in the O2 run the detectors showed marginally less

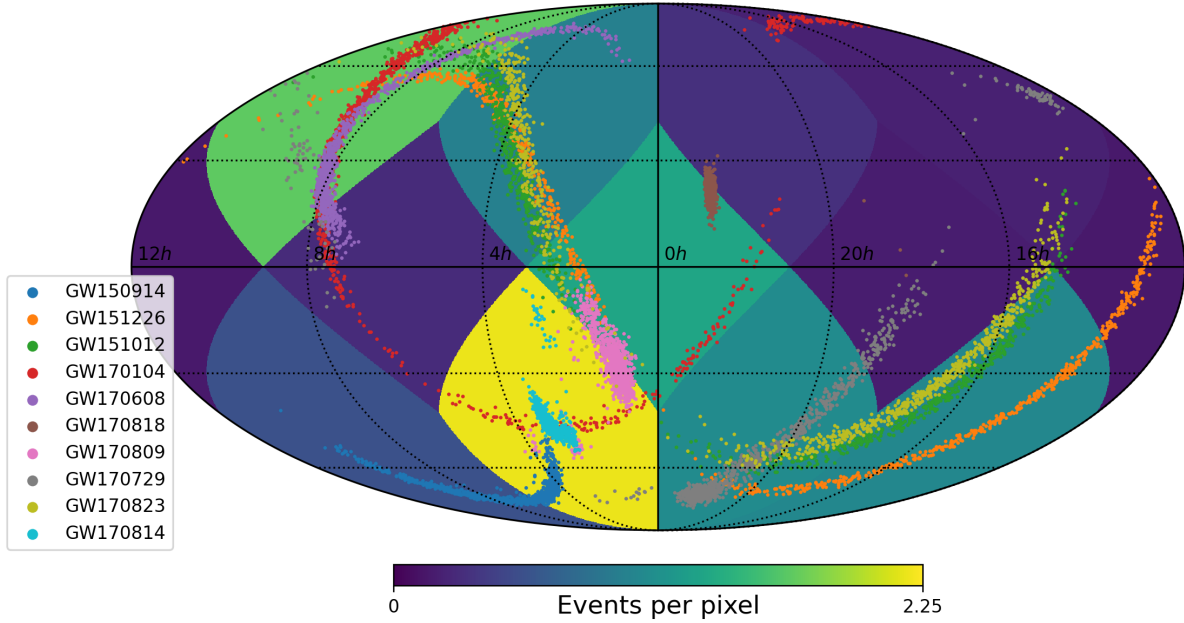


Figure 1. A sky map divided into 12 pixels of equal area, the colour scale indicates the number of events per pixel (calculated by counting the number of posterior samples in each pixel, normalised by the total number of samples per event). About ~ 2.2 events are assigned to the highest density pixel as GW170814 and partially GW170809 are tightly localised to that pixel. Some pixels contain almost no samples; the pixel with the largest fraction of events contains ~ 15 times more samples than the pixel with the smallest fraction.

preference for certain directions. This can be explained by the increased up-time of the O2 run, which reduces the overall variation in right ascension.

Fig. 2 shows the resulting selection functions (probability of detection) for O1 and O2 are plotted as a function of distance for multiple sky positions. This shows the effect described above, with anisotropic variations favouring the latitudes directly above the LIGO detectors, but with the response function smeared out in right ascension by the Earth’s rotation. Nonetheless there is still some variation in right ascension, which is more pronounced for the O1 run. Comparing the two panels also shows the overall increase in detection sensitivity in the O2 run.

Marginalising out the distance we obtain the probability of detection as a function of right ascension and declination. To calculate the probability of detection at the time of events we use the PSD estimate at the time of the BBH merger. This, along with the merger time, fully specifies the orientation of the network geometry in an Earth-fixed coordinate system which rotates in time along with the Earth. Examples of the probability of detection function for GW151226 and GW170104 are shown in Fig. 3. The figure also shows the bright spots of high probability from which a detection would be expected and the relative increase in sensitivity (about one order of magnitude) between the two runs. The probability of detection maps are rendered on a higher dimensional map (3072 pixels) compared to the 12-dimensional map of pixel weights.

We only use the LIGO Hanford-Livingston detector network for this analysis since these were the only 2 detectors used to determine detection in the O1 and O2 runs (Abbott et al. 2019b), the Advanced Virgo detector (Acernese et al. 2014) only joined at the end of the O2 run. However, despite Virgo’s lower sensitivity during O2 relative to the LIGO detectors, addition of its data for, for example, GW170814 (Abbott et al. 2017b) yielded significantly better localisation compared to the earlier detections.

Pixel weight a_i	$[0, 150] \text{ Gpc}^{-3} \text{ yr}^{-1} \text{ sr}^{-1}$
Total astrophysical rate R	$[10^{-5}, 750] \text{ Gpc}^{-3} \text{ yr}^{-1}$
First Euler angle about the z -axis α	$[0, 2\pi]$
Second Euler angle about the y -axis $\cos \beta$	$[0.75, 1]$
Third Euler angle about the z -axis γ	$[0, 2\pi]$

Table 1. Prior ranges on inferred parameters $\vec{\theta}$ and the total rate R .

2.2 Prior

In the isotropic case, the only free parameter of the model is R , the overall rate of mergers measured in $\text{Gpc}^{-3} \text{ yr}^{-1}$. We choose a Jeffreys prior,

$$p(R|\text{ISO}) \propto R^{-1/2}, \quad (5)$$

which allows a direct comparison with rate estimates published by the LIGO-Virgo Collaboration using sophisticated measurements of sensitive time-volume and models of the source population (Abbott et al. 2019c).

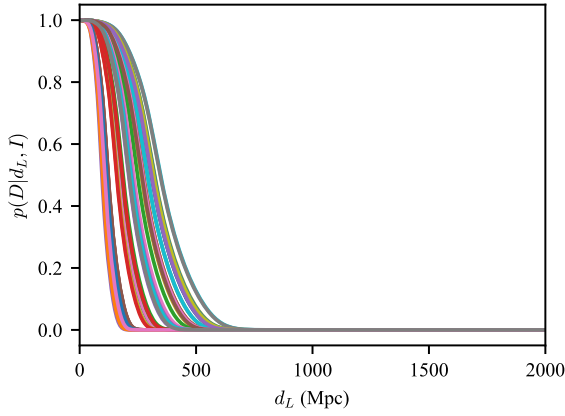
For the anisotropic model with N equal-area pixels, we have parameters $a_1 \dots a_N$. Since we wish to compare to the isotropic model, we specify the prior on the overall rate R (Eq. 2) to have the same Jeffreys form as Eq. 2.2, so

$$p(R|\text{ANISO}) \propto R^{-1/2} \propto \int p(R|\vec{a}) p(\vec{a}|\text{ANISO}) d^N \vec{a}.$$

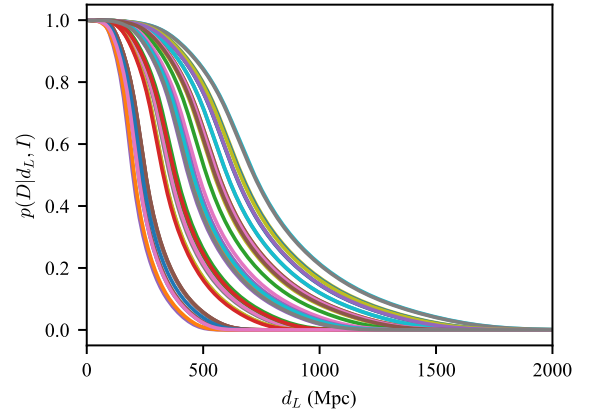
Since we do not favour any particular pixel a-priori it should be symmetric in $a_i \leftrightarrow a_j$. The following prior fulfils this criteria, while being uniform on the $N - 1$ -simplex of possible \vec{a} s for a particular R ,

$$p(\vec{a}|\text{ANISO}) \propto \left(\sum_i^N a_i \right)^{-(2N-1)/2}.$$

Boundaries found in Table 1 are applied to the inferred pa-



(a) Survival function for O1



(b) Survival function for O2

Figure 2. Comparison of survival functions for the O1 (a) and O2 (b) runs, where each line is the survival function sampled at a discrete sky position. The detectors are most sensitive towards directions above and below, and least sensitive to directions in the plane of the detector. There is a significant increase in sensitivity between the two runs.

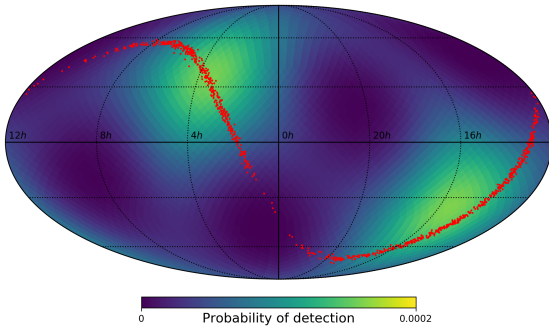
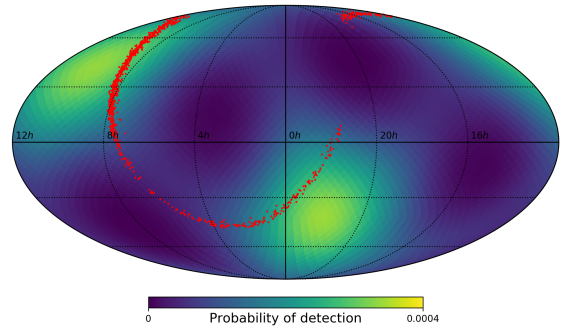
(a) $p(D|\Omega, I)$ at the time of GW151226.(b) $p(D|\Omega, I)$ at the time of GW170104.

Figure 3. Probability of detection maps at the time of GW151226 (a) from O1 run and GW170104 from O2 run (b), with the respective posterior samples scattered over. The maps were calculated with the PSD at the time of event detection and marginalising the selection function over distance. While the pattern is the same due to presence of only two LIGO detectors, the magnitude of the detection probability increases for GW170104 as the detectors were more sensitive during the O2 run.

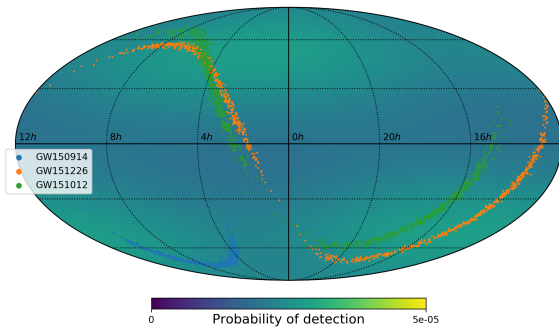
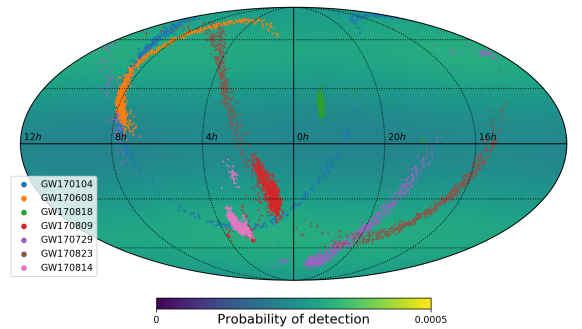
(a) Mean $p(D|\Omega, I)$ for the O1 run(b) Mean $p(D|\Omega, I)$ for the O2 run

Figure 4. Mean probability of detections maps for the O1 (a) and O2 (b) runs, with posterior samples for events from O1 and O2 scattered over. The maps were calculated with the average PSD for each run, marginalising the selection function over distance and time averaging the $p(D|\Omega, t, I)$, where t is the GPS time, over the times the detectors were operational.

rameters. Note that the boundary on the total rate R is well outside of the range found by the O1 and O2 run (Abbott et al. 2019c). The Euler angles rotate the angular distribution of pixels, however without restricting the range of rotations the posterior would become strongly degenerate as multiple combinations of the Euler angles would correspond to the identical orientation of the HEALpix grid. Our intent in setting the boundaries for the Euler angles is twofold. First, we choose a uniform prior over the ranges as shown in Table 1. Second, to avoid degeneracy of the likelihood we enforce a condition wherein no pixel centre can be rotated beyond its original boundary. An example of this degeneracy is rotating the pixel grid about the z -axis by an angle that corresponds to the angular separation of two nearby pixel centres that lie in the $x-y$ plane. The range of $\cos\beta$ was restricted (Table 1) as values outside this range would violate the aforementioned second condition.

2.3 Likelihood

In our specific problem, the likelihood function $p(N_{\text{obs}}, \{x_j\} | \vec{\theta}, I)$ depends on the data for each detected event (yielding estimates of their sky position and distance) and the selection function. The likelihood can be split into so called number and event likelihood respectively (Mandel et al. 2018),

$$p(N_{\text{obs}}, \{x_j\} | \vec{\theta}, D, I) = P(N_{\text{obs}} | \vec{\theta}, \hat{D}, I) p(\{x_j\} | \vec{\theta}, D_j, I), \quad (6)$$

where \hat{D} indicates the use of the averaged selection function over the period of the observing run and D_j indicates the selection function evaluated using the state of the detector network at the time of the j th detection. Furthermore, the number likelihood is a Poisson process, thus we can use the marginalisation rule to introduce the expected number of detections \hat{N} , such that

$$P(N_{\text{obs}} | \vec{\theta}, \hat{D}, I) = \int P(N_{\text{obs}} | \hat{N}, I) p(\hat{N} | \vec{\theta}, \hat{D}, I) d\hat{N}.$$

The first term on the right hand side of the equation above is the Poisson probability of N_{obs} given the expected number \hat{N} . The second term, the probability density function of the expected number, is the Dirac delta function at \hat{N}_R , which is determined by the average rate of BBHs mergers and the interferometers' selection function, hence

$$P(N_{\text{obs}} | \vec{\theta}, \hat{D}, I) = P(N_{\text{obs}} | \hat{N} = \hat{N}_R, I) = \frac{\hat{N}_R^{N_{\text{obs}}}}{N_{\text{obs}}!} e^{-\hat{N}_R}. \quad (7)$$

To compute the expected number of detections \hat{N}_R , we integrate the product of the selection function and the expected density of detections over time and volume. Since the detectors are not equally sensitive in all directions, and the detection probability falls off at higher distances, this selection is crucial in obtaining a correct estimate for our purposes of finding any anisotropy. We can think of this as the observable fraction of the actual number of mergers $N_{\text{merg}} = RVT$, where R is the average rate per space-time volume as defined in Eq. (2), V is the volume, and T the observation time. Since the detection probability vanishes at sufficiently high distances, our result will be independent of the choice of V provided we consider a volume much larger than the observable one. We note that for this analysis we have assumed a distance prior $\sim d_L^2$ where d_L is the luminosity distance, which is consistent with a Euclidean universe. We have also assumed an underlying astrophysical rate that is constant with distance (and therefore with redshift). Since our primary aim is to test anisotropy (and not homogeneity) coupled with the fact that our detections are positioned in the local universe

we expect that the impact of these assumptions (which are shared by both models) to be a second order effect. The expected total number of detections is given by

$$\begin{aligned} \hat{N}_R &= N_{\text{merg}} \iint \frac{\partial^2 N_{\text{obs}}}{\partial \Omega \partial d_L} dd_L d\Omega \\ &= RVT \iint p(\hat{D} | \Omega, d_L, I) p(\Omega, d_L | \vec{a}, I) dd_L d\Omega \\ &= RVT \int p(\hat{D} | \Omega, I) p(\Omega | \vec{a}, I) d\Omega, \end{aligned} \quad (8)$$

where the distance d_L is marginalised out in the last step and $p(\hat{D} | \Omega, I)$ is the probability of detection as a function of sky position averaged over the times when the interferometers were operating. The expected number of events is evaluated separately for O1 and O2, as the selection function and observation time differ for each run.

The event likelihood in Eq. (6) can be split into a product over all events, since we assume they are independent of each other,

$$p(\{x_j\} | \vec{a}, D_j, I) = \prod_j^{N_{\text{obs}}} p(x_j | \vec{a}, D_j, I).$$

This can be further expressed using Bayes's theorem, the marginalisation rule and noting that $p(D_j | x_j, \vec{a}, I) = 1$ for the detections. The prior and evidence in Eq. (9) can be expanded by marginalising over distance and solid angle, giving us

$$\begin{aligned} p(x_j | \vec{\theta}, D_j, I) &= \frac{p(x_j | \vec{\theta}, I)}{p(D_j | \vec{\theta}, I)} \\ &= \frac{\int d\Omega \int d_L p(x_j | \Omega, d_L, I) p(\Omega, d_L | \vec{\theta}, I)}{\int d\Omega \int d_L p(D_j | \Omega, d_L, I) p(\Omega, d_L | \vec{\theta}, I)} \\ &\approx \frac{\frac{1}{N} \sum_k^N p(\Omega_{j,k}, d_{L,k} | \vec{\theta}, I)}{\int d\Omega p(D_j | \Omega, I) p(\Omega | \vec{\theta}, I)}, \end{aligned} \quad (9)$$

where in the final step we evaluate the integral in the numerator via Monte Carlo approximation over the GWOSC posterior samples (indexed by k), and marginalise out distance in the expression in the denominator,

$$p(D_j | \Omega, I) = \int d_L p(D_j | \Omega, d_L, I) p(d_L | I),$$

as we assume that the probability of a source originating from a given sky area (pixel) is independent of the distance,

$$p(\Omega, d_L | \vec{a}, I) = p(\Omega | \vec{a}, I) p(d_L | I). \quad (10)$$

The selection function $p(D_j | \Omega, I)$ is taken to be the value at the time of detection of the j th event and the probability density function of a sky position within the i th pixel is taken to be uniform within the pixel and proportional to the pixel weight a_i . As mentioned earlier, we also assume that the prior on the distance is proportional to its square, thus we are only considering a static Euclidean universe in this simplified model.

3 RESULTS

The isotropic model is parametrised only by a single pixel, which spans the entire sky, making it invariant under the angular distribution of pixels and independent of the Euler angles. On the other hand, the anisotropic model consists of a 15-dimensional parameter

Anisotropic model total rate \hat{R}_{ani}	$64.9^{+36.1}_{-32.4} \text{ Gpc}^{-3} \text{ yr}^{-1}$
Isotropic model total rate \hat{R}_{iso}	$60.5^{+40.5}_{-24.3} \text{ Gpc}^{-3} \text{ yr}^{-1}$
LVC total rate	$53.2^{+58.5}_{-28.8} \text{ Gpc}^{-3} \text{ yr}^{-1}$
Bayes factor $Z_{\text{ISO}}/Z_{\text{ANISO}}$	$\sim 16 : 1$

Table 2. Comparison of the total rate of our models with the LVC result and the Bayes factor ratio of the isotropic and anisotropic model.

space. Each posterior sample for the anisotropic case contains a set of pixel weights and the associated Euler angles describing the orientation of the HEALPix grid. It follows then that in each sample the pixels will correspond to different locations on the sky, which is accounted for before averaging the pixel weights. In Fig. 6 we show the maximum likelihood probability sample. To average the pixel weights, the original 12 pixels are split to a set of 12,288 pixels which map the samples onto a finer basis, while preserving their respective values. This larger set is rotated and then averaged out as this corresponds to returning to the original coordinate system, resulting in smoothing of the original 12-dimensional pixel basis and rendering the mean pixel weights on a higher-dimensional map.

The averaged pixel map of posterior samples for the anisotropic model is shown in Fig. 7. Two parts of the sky have above average values of rate density, corresponding to the areas with the highest density of samples (Fig. 1). However, the ratio of the maximum to the minimum rate densities is ~ 3 , while the ratio of the maximum to the minimum number of GW event posterior samples per pixel is ~ 15 (Fig. 1), illustrating how the selection functions differs between the sampling of the posterior and a simple samples count.

Furthermore, we obtain estimates of the total rate R (defined in Eq. 2) as in our analysis the rate is conditionally dependant upon the pixel weights. In Fig. 5 we show the histogram of the total rate and compare the results for our two models. We quote our results with 90% credibility intervals in Table 2. The confidence intervals we obtain are marginally tighter than the LVC estimate of the total rate (Abbott et al. 2019c). This difference can be attributed to a number of differing assumptions between the LVC analysis and our own. These include, but are not limited to the facts that: our analysis makes different prior assumptions about the black hole mass distribution, and that we do not marginalise over uncertainty in the mass power law index and our model assumes a maximum total mass. In addition, we have not used a realistic cosmological model for our redshift distribution, we have considered only the inspiral component of the signal waveform as opposed to the full inspiral, merger, and ringdown, and our selection function is computed analytically and not empirically from simulated signal injections into real non-Gaussian detector noise.

To answer the question of whether the BBH mergers are distributed isotropically on the sky, we calculate the Bayes factor between the two hypotheses by taking ratios of the evidences of our two models (defined in Eq. 3). We arrive at a Bayes factor of $\sim 16 : 1$ in favour of the isotropic model, indicating that the 10 events from O1 and O2 runs are better described by the isotropic model.

Lastly, to test our model we replace the 10 events from O1 and O2 with 10 copies of GW170814, simulating an anisotropic scenario wherein all GW events come from the same location. The resulting Bayes factor in this case is $\sim 10^5$ in favour of the anisotropic model.

4 CONCLUSION

We perform a Bayesian model selection analysis comparing an isotropic and anisotropic, pixellated, models of the BBH astrophysi-

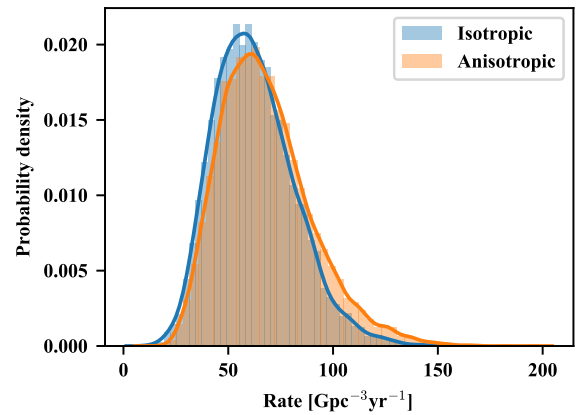


Figure 5. Posterior probability distributions on the rate R of BBH mergers, assuming the isotropic and anisotropic models. The results are consistent with the LVC estimate of the total rate $53.2^{+58.5}_{-28.8} \text{ Gpc}^{-3} \text{ yr}^{-1}$ of BBH mergers

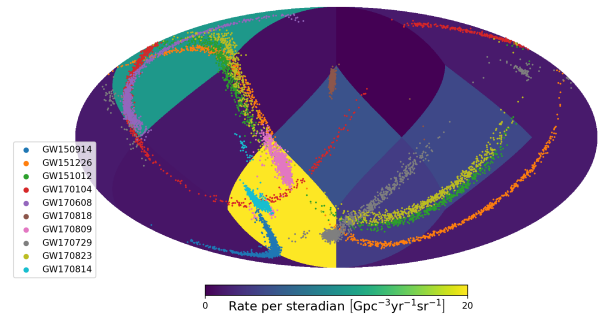


Figure 6. Example of a posterior sample for the anisotropic model, corresponding to the maximum likelihood probability. The GW event samples are rotated relative to the original coordinate system (Fig. 1).

cal rate. We show that the 10 detected BBH events from O1 and O2 runs are sufficient in favouring the a priori expected isotropic model with a Bayes factor of $\sim 16 : 1$. This result was expected as the underlying distribution of BBH mergers is thought to be isotropic, however with only 10 events forming our measured dataset a strong statement about isotropy should not be expected. Nevertheless, with the ongoing O3 run more events will become available for this analysis and, furthermore, the O3 events should be better localised due to sensitivity improvements at the Virgo site. Thus, in the future we predict that this work can be used to significantly strengthen our belief in the isotropic model over an anisotropic model as the number of detections increases. Alternatively, the analysis can be interpreted as an important probe for finding anisotropies should they exist.

The anisotropic model is described with 15 parameters which gives a very large parameter space for the model, most of which is incompatible with the data. Since we made a decision to use a pixel basis and the minimum number of pixels a HEALpix map supports is 12 it was not possible to easily switch to a lower dimensional basis. Thus, one of the future possibilities of this project would be to perform this analysis in a spherical harmonic basis. A spherical harmonic basis would potentially allow for a lower dimensional parameter space, for example, the simplest anisotropic spherical harmonic model would have 4 weight parameters (polynomial degree $l_{\text{max}} = 1$). Such spherical harmonic approaches could be readily

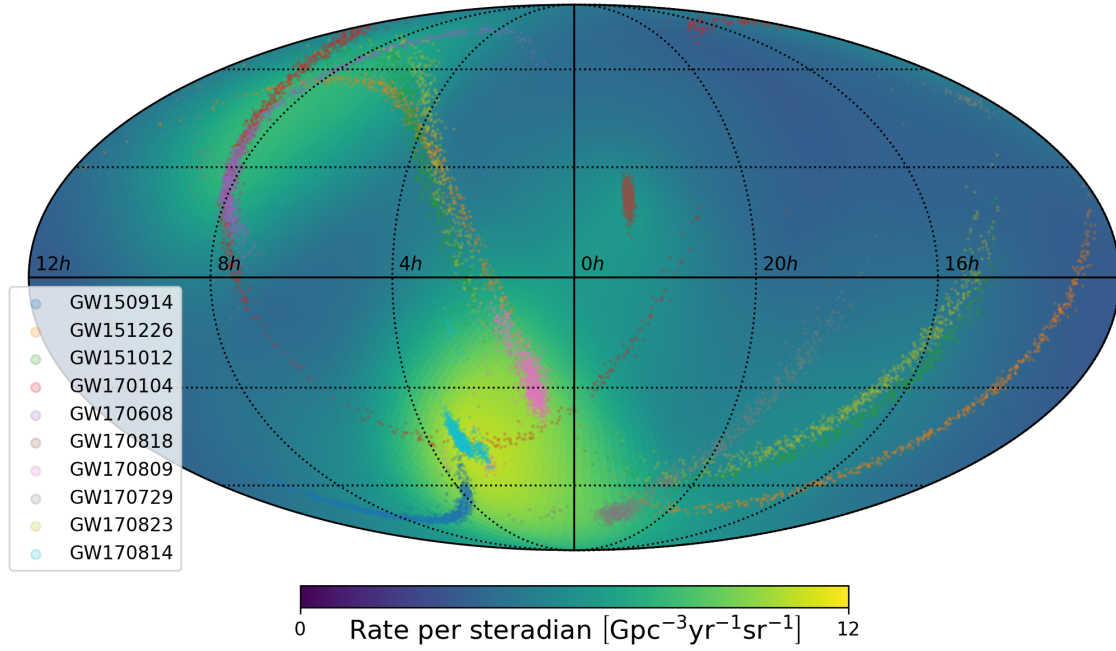


Figure 7. A mean map of pixel weights averaged over the different rotations of the posterior distributions such as Fig. 6. The individual samples were rendered on a smoother basis of 12288 pixels (the weights are defined per steradian, thus independent of the pixel size), rotated to a default frame of reference and averaged. The ratio of the maximum to the minimum rate density of the map is ~ 3 .

used to model different anisotropy models, providing us with an alternative representation with which to compare the benchmark isotropic model.

Also, in this analysis the prior probability density function (PDF) on luminosity distance is consistent with that of a simple, static Euclidean universe. As the interferometers are being upgraded in terms of sensitivity it would be reasonable to include a cosmological model of an expanding universe since some events are already at significant redshifts. However, we do not expect this to change the result dramatically, rather it should result in scaling the selection function and providing us with better tools that could be used in further applications. Finally, and potentially most importantly, at the time of writing, only ten events (from O1 and O2) have been published by the LIGO-Virgo Collaboration. The ongoing O3 run is living up to expectations and has provided ~ 40 additional candidates to date (LIGO-Virgo Collaboration 2020). Such additional data will only serve to strengthen the analysis presented here and we are eager to use these events to compare our BBH distribution models. In the limit of large numbers of detections, if BBH sources trace the large scale structure of the universe we might expect that a general anisotropic model might be favoured over isotropy. This scenario would allow us to meaningfully compare our results to the distribution of visible matter in the universe.

ACKNOWLEDGEMENTS

This work was supported by a Royal Astronomical Society summer undergraduate research bursary. We thank Rachel Gray for useful discussions. This research has made use of data, software and/or web tools obtained from the Gravitational Wave Open Science Center (<https://www.gw-openscience.org>), a service of LIGO Laboratory, the LIGO Scientific Collaboration and the Virgo Collaboration. LIGO is funded by the U.S. National Science Foundation.

Virgo is funded by the French Centre National de Recherche Scientifique (CNRS), the Italian Istituto Nazionale della Fisica Nucleare (INFN) and the Dutch Nikhef, with contributions by Polish and Hungarian institutes. JV was partially supported by STFC grant ST/K005014/1 and JV and CM are supported by the Science and Technology Research Council (grant No. ST/L000946/1).

REFERENCES

- Abbott B. P., et al., 2016a, *Phys. Rev. X*, 6, 041015
- Abbott B. P., et al., 2016b, *Phys. Rev. Lett.*, 116, 061102
- Abbott B. P., et al., 2016c, *Astrophys. J. Lett.*, 833, L1
- Abbott B. P., et al., 2017a, *Phys. Rev. Lett.*, 118, 221101
- Abbott B. P., et al., 2017b, *Phys. Rev. Lett.*, 119, 141101
- Abbott B. P., et al., 2017c, *Ap. J. Lett.*, 851, L35
- Abbott B. P., et al., 2018, *Living Rev. Rel.*, 21, 3
- Abbott B. P., et al., 2019a, preprint ([arXiv:1908.06060](https://arxiv.org/abs/1908.06060))
- Abbott B. P., et al., 2019b, *Phys. Rev.*, X9, 031040
- Abbott B. P., et al., 2019c, *Astrophys. J.*, 882, L24
- Acernese F., et al., 2014, *Classical and Quantum Gravity*, 32, 024001
- Anderson W. G., Brady P. R., Creighton J. D. E., Flanagan E. E., 2001, *Phys. Rev. D*, 63, 042003
- Chen H.-Y., Essick R., Vitale S., Holz D. E., Katsavounidis E., 2017, *Astrophys. J.*, 835, 31
- Daniel Sigg 2016a, H1 Calibrated Sensitivity Spectra Oct 24 2015 (Representative for O1), <https://dcc.ligo.org/LIGO-G1600150/public>
- Daniel Sigg 2016b, L1 Calibrated Sensitivity Spectra Oct 24 2015 (Representative for O1), <https://dcc.ligo.org/LIGO-G1600151/public>
- Dominik M., Berti E., O’Shaughnessy R., Mandel I., et al., 2015, *ApJ*, 806, 263
- Górski K. M., Hivon E., Banday A. J., Wandelt B. D., Hansen F. K., Reinecke M., Bartelmann M., 2005, *ApJ*, 622, 759
- Harry G. M., 2010, *Class. Quant. Grav.*, 27, 084006
- Horvath I., Hakkila J., Bagoly Z., 2013, arXiv e-prints, p. [arXiv:1311.1104](https://arxiv.org/abs/1311.1104)
- LIGO Scientific Collaboration 2015, *Class. Quantum Grav.*, 32, 074001

- LIGO-Virgo Collaboration 2018, GWTC-1, <https://dcc.ligo.org/LIGO-P1800374/public>
- LIGO-Virgo Collaboration 2019, Power Spectral Densities (PSD) release for GWTC-1, <https://dcc.ligo.org/LIGO-P1900011/public>
- LIGO-Virgo Collaboration 2020, Gravitational-Wave Candidate Event Database, <https://gracedb.ligo.org/superevents/public/03/>
- Mandel I., Farr W. M., Gair J. R., 2018, preprint, ([arXiv:1809.02063](https://arxiv.org/abs/1809.02063))
- Ng K. K. Y., Vitale S., Zimmerman A., Chatziioannou K., Gerosa D., Haster C.-J., 2018, *Phys. Rev.*, D98, 083007
- O’Shaughnessy R., Vaishnav B., Healy J., Shoemaker D., 2010, *Phys. Rev. D*, 82, 104006
- Saadeh D., Feeney S. M., Pontzen A., Peiris H. V., McEwen J. D., 2016, *Phys. Rev. Lett.*, 117, 131302
- Singer L. P., Price L., 2016, *Phys. Rev. D*, 93, 024013
- Skilling J., 2006, *Bayesian Anal.*, 1, 833
- Vallisneri M., Kanner J., Williams R., Weinstein A., Stephens B., 2015, in *Journal of Physics Conference Series*. p. 012021 ([arXiv:1410.4839](https://arxiv.org/abs/1410.4839)), doi:10.1088/1742-6596/610/1/012021, <https://www.gw-openscience.org/about/>
- Veitch J., et al., 2015, *Phys. Rev. D*, 91, 042003
- Veitch J., Del Pozzo W., Cody Pitkin M., ed1d1a8d 2017, <http://www.github.com/johnveitch/cpnest>, doi:10.5281/zenodo.835874, <https://doi.org/10.5281/zenodo.835874>
- Virgo Collaboration 2014, *Class. Quantum Grav.*, 32, 024001